Unravelling the critical role of silanol in Pt/SiO_2 for room temperature HCHO oxidation: An experimental and DFT study

Shuo Chen [a], Saber Gueddida [b], Michael Badawi [b], Sébastien Lebègue [b], Jean-Marc Giraudon [a], Jérémy Dhainaut [a], Sébastien Royer [a,*], Jean-Francois Lamonier [a,*]

[a] Univ. Lille, CNRS, Centrale Lille, Univ. Artois, UMR 8181, UCCS, Unité de Catalyse et Chimie du Solide, Lille F-59000, France
[b] Université de Lorraine, CNRS, Laboratoire de Physique et Chimie Théoriques, UMR 7019, Nancy F-54000, France

ARTICLE INFO

ABSTRACT

In the present work, Pt/SiO_2 catalysts have been prepared by impregnating as-prepared Pt NPs onto commercial SiO_2 of tailored silanol density (2.3, 3.1 and 4.5 OH nm^{-2}) produced through hexamethyldisilazane passivation. The resulting Pt/SiO_2 catalysts were then tested for formaldehyde (HCHO) total oxidation. The catalytic tests showed that high surface silanol density led to lower apparent activation energy (from 40.7 kJ·mol^{-1} at 2.3 OH nm^{-2} to 21.9 kJ·mol^{-1} at 4.5 OH nm^{-2})), allowing formaldehyde total oxidation in dry and wet conditions (100% conversion into CO_2 over Pt/SiO_2 (4.5 OH nm^{-2}) at room temperature in dry condition, among the best catalytic performances reported). DFT calculations described the different interaction behaviours of HCHO, H_2O, CO and CO_2 on pure SiO_2 and Pt/SiO_2 (1.1–7.2 OH nm^{-2}) surface, showing the critical role of silanols in the total oxidation of formaldehyde over Pt/SiO_2 in different humid conditions.

1. Introduction

Formaldehyde (HCHO) is a dominant indoor air pollutant, which is usually emitted from building and furnishing materials, plastic cements, paints, and other consumer products, and is harmful to human health even at a very low concentration [1]. Various approaches have been developed to reduce indoor HCHO pollution, including the manifold recovery technologies (e.g., adsorption, absorption, membrane separation, and condensation) and oxidative approaches (catalytic oxidation, thermal incineration, biological degradation, photocatalytic decomposition, and non-thermal plasma oxidation), among which the catalytic oxidation stands out since it's environmentally friendly and cost-effective [2]. Up to date, numerous metal oxide catalysts (Ce, Mn, Co, Ni) and noble metal (Pt, Au, Pd, Ir, Rh) catalysts have been developed for HCHO total oxidation [3–8]. Among them, Pt based catalysts stabilized by different supports, metal oxides in most cases (e.g., TiO_2, CeO_2, MnO_2, Co_3O_4, and Al_2O_3), have attracted much attention due to their excellent catalytic performance at room temperature [9–13]. The high catalytic reactivity of Pt-based catalysts has been well correlated to the fine dispersion of Pt sites, the high reducibility of the metal oxide supports, and the existence of rich surface oxygen vacancies [2]. However, the high cost of noble metal catalysts has limited their practical

application. Therefore, there is still a need to further improve their catalytic performance or to reduce their application cost.

Silica, one main support for metal supported catalysts, has been widely used thanks to its good thermal stability, tunable porosity and low cost [14]. However, due to the absence of any red-ox properties, silica has been considered as a poor support for low temperature HCHO oxidation [2]. For instance, an early report showed that the catalytic performance of Pt/SiO_2 was unsatisfied for low-temperature HCHO total oxidation, requiring either heating or high Pt loading (1 wt%) for a complete HCHO decomposition [15]. Though a following work showed that the catalytic performance of Pt/SiO_2 could be enhanced via improving metal dispersion, the use of silica as support still has been rarely considered in literature to date [16].

Surface hydroxyl groups, having a profound influence on the catalyst surface environment, play a key role in HCHO decomposition. Zhang et al. [17] reported that the surface hydroxyls close to noble metal particles could alter the HCHO oxidation pathway from the HCHO decomposition followed by CO oxidation (HCOO-M → CO-M + OH-M)) to that of direct formate oxidation (HCOO-M + OH-M → H_2O + CO_2 + 2 M). Additional favourable effects of surface hydroxyls include promoting HCHO adsorption and diffusion of the intermediates [9,18]. Since their beneficial effects was first revealed over Pt/TiO_2, a series of

Pt-based catalyst has been designed to take advantage of the surface hydroxyls for low temperature HCHO decomposition, either using hydroxyl-enriched supports (e.g., AlOOH, CeO_2-AlOOH, SiO_2-AlOOH, MnO_2/AlOOH, MnO_2/Ni(OH)$_2$) [10,11,19,20], adding additives (e.g., Pt-O(OH)$_x$ alkali-metal species, Pt-Ni(OH)$_x$) [12,17,18,21], or directly introducing water to the reaction system [22]. A recent work by Li et al. [18] showed that the incorporation of the hydrophilic silicate in Pt/SiO$_x$-TiO$_2$ could maintain a wet microenvironment on catalyst surface, which benefited HCHO decomposition at low temperature and in dry environment.

The critical role of surface hydroxyl groups as well as the importance of hydrophobicity of the support inspires the possibility to take advantage of the silanol groups of the amorphous silica as support for HCHO oxidation, despite the absence of red-ox properties. It is widely agreed that the type and concentration of silanol groups on a SiO_2 surface play a vital part in the interaction of between SiO_2 and the supported active metal sites [23], as well as in the adsorption of the reactants, intermediates and products during the catalytic reaction, all of which have an important influence on the reaction mechanism [24]. However, it is still not clear about the part of the silanol groups in SiO_2 in HCHO oxidation so far.

The present work aims at to investigating impacts of the silanol content in Pt/SiO$_2$ on the catalyst surface properties and the interaction between silanol with the reaction gases during HCHO oxidation. This pioneer work is beneficial for fundamental understanding of HCHO oxidation from a new point of view and the rational design of efficient catalysts for the reaction. Herein, we prepared a series of SiO$_2$ with tailored the silanol density (2.3, 3.1 and 4.5 OH nm^{-2}) via the hexamethyldisilazane passivation, and further used to support well-controlled Pt NPs with the same metal dispersion and valent state. This rational design allows us to reveal the role of Si-OH in Pt/SiO$_2$ in HCHO oxidation by combining experimental and DFT studies. It was proved that the silanol contents significantly affected the interaction behaviours of HCHO, H$_2$O, CO and CO$_2$ with the catalyst surface, which in turn determined the catalytic performance of Pt/SiO$_2$ under different humid conditions. The silanol-rich Pt/SiO$_2$ even with low Pt loading (0.2 wt%) is highly efficient and stable in HCHO oxidation at room temperature, which makes it promising for the removal of indoor HCHO. The present work carefully investigates Pt/SiO$_2$ surface environment in relation with formaldehyde oxidation mechanisms.

2. Experimental section

2.1. Materials and reagents

Hexamethyldisilazane (Sigma-Aldrich, ≥99%), H$_2$PtCl$_6$·6H$_2$O (Sigma-Aldrich, 37.50% Pt basis), ammonia water (Thermo scientific, 28%), toluene (Sigma-Aldrich, anhydrous, 99.8%), ethylene glycol (Sigma-Aldrich, 99.8%), NaOH (Sigma-aldrich, >98%), HCl (Sigma-Aldrich, ACS reagent, 37%), ethanol (Sigma-Aldrich, pure), poly-vinylpyrrolidone (Sigma-Aldrich, M$_w$ = 29,000), commercial silica from Saint-Gobain Norpro, SiC from Thermo scientific. All chemical reagents are of analytical grade and have been used without further purification.

2.2. Catalyst preparation

2.2.1. Preparation of SiO$_2$ supports

Silica with various surface silanol densities (SiO$_2$-x, x representing Si-OH density evaluated using several characterization techniques as discussed in Section 3.1) were obtained through different treatment strategies as follows: First the silanol-rich silica was prepared via the base treatment: 1 g silica was merged in 15 mL ammonia water for 1.5 h at 25 °C, followed by filtration, sufficient washing with deionized water and overnight drying at 80 °C. This sample is indexed as SiO$_2$-4.5. Then SiO$_2$-4.5 was used as the starting material to prepare silica with less silanol popularities through the silylation reactions of OH with

hexamethyldisilazane (HMDS). To prepare SiO$_2$-3.1, 0.5 g SiO$_2$-4.5 was pretreated under vacuum at 150 °C for 3 h to clean the silica surface, and then dispersed in 15 mL toluene to form a homogenous silica suspension, in which 50 μL HMDS in toluene was dropped. The silylation reaction lasted for 6 h at 25 °C under stirring (300 rpm). The passivated SiO$_2$ was collected via centrifugation (9000 rpm, 15 min), thoroughly washed with acetone, and dried at 150 °C under vacuum for 12 h. The procedure to prepare SiO$_2$ with low silanol density (SiO$_2$-2.3) is the same with SiO$_2$-3.1, except that excessive HMDS (100 μL) was added to consume the maximum quantity of silanol of SiO$_2$-4.5.

2.2.2. Preparation of Pt nanoparticles and Pt/SiO$_2$ catalysts

Pt nanoparticles were prepared via ethylene glycol (EG) reduction method [25]. Typically, 0.05 g H$_2$PtCl$_6$·6 H$_2$O in 20 mL EG was dropped into 20 mL of a NaOH (0.22 g) /EG solution. A transparent yellow suspension was obtained after 1 h, which was then heated at 90 °C for 2 h with a N$_2$ flow passing through the reaction system until a transparent dark-brown colloidal solution was obtained without any precipitate. The Pt nanoparticles were precipitated by adding 18 mL HCl solution (0.3 M), collected by centrifugation (10,000 rpm, 15 min) and dispersed in ethanol.

Pt/SiO$_2$ catalysts were prepared via wet impregnation. Typically, a certain amount of SiO$_2$-x powder was immersed in 15 mL ethanol containing an appropriate amount of as-prepared Pt nanoparticles solution and stirred at 25 °C for 12 h. After centrifugation (10,000 rpm, 15 min), the sample was washed with ethanol, air-dried at 25 °C, calcined at 350 °C for 12 h and reduced in H$_2$ at 300 °C for 2 h with a ramp of 1.5 °C/min and 1 °C/min, respectively. Resulting samples were indexed as PtSiO$_2$-x, with x = 2.3, 3.1, 4.5.

2.3. Sample characterization

Powder X-ray diffraction (PXRD) patterns were collected on a Bruker D8 Advanced AXS diffractometer. The diffractometer was operated at 40 kV and 30 mA and was equipped with a monochromatic Cu Kα radiation source (λ = 1.5418 Å). Step time of 1 s and step size of 0.02° was applied to record the X-ray diffractograms. The average diameters of Pt NPs in ethanol were determined by Dynamic Light Scattering (DLS, Nano ZS from Malvern Instruments). N$_2$ physisorption experiments were performed at − 196 °C on a Micromeritics Tristar II Plus instrument. Before analysis, samples were degassed at 150 °C for 12 h. Textural properties were calculated from the adsorption/desorption isotherms by using Tristar II software version 1.55. Pt contents in samples were evaluated using an Agilent Technologies 700 Series inductively coupled plasma-optical emission spectrometer (ICP-OES). The materials were dissolved in concentrated HCl/HNO$_3$ mixture before analysis. Contents of carbon element of SiO$_2$-3.1 and SiO$_2$-2.3 were evaluated using a Carlo-Erba CHNS-11110 equipment. Before analysis the samples were carefully cleaned up via drying at 150 °C under vacuum overnight to remove any possible solvent or HMDS residues.

High angle annular dark field (HAADF) imaging and scanning transmission electron microscopy–energy dispersive X-ray spectroscopy (STEM-EDX) have been conducted using a FEG TEM/STEM system (Titan Themis FEI) operated at 300 kV. The microscope is equipped with a monochromator, a super-X windowless fourquadrant silicon drift detector (SDD) for the STEM-EDX mapping, and a probe Cs corrector allowing spatial resolution of about 65 pm. For both HAADF acquisitions and STEM-EDX mapping, the probe size was about 500 pm with screen currents comprised between 50 and 100 pA. Collection angles for the HAADF detector were comprised between 50 and 200 mrad. For the probe, a semi-convergence angle of 21 mrad was Journal Pre-proof 10 used. Samples were directly observed as powders.

High resolution X-ray Photoelectron Spectra (XPS) were collected on a Kratos Analytical AXIS Ultra DLD spectrometer equipped with a monochromatic Al Kα X-ray source (hν = 1486.6 eV) and a charge compensation gun, with a constant pass energy of 20 eV. The spectra

were obtained after the samples were purged at room temperature under vacuum. Spectral decomposition and quantification were done using CasaXPS, after calibration with adventitious C1s (284.8 eV). The FT-IR spectra were recorded on an infrared spectrometer in the attenuated total reflectance mode (IR-ATR) from Thermo Scientific (IS50) over the range of 4000–400 cm^{-1}. Before analysis the samples were pretreated at 150 °C under vacuum to remove humidity. Thermogravimetry (TG) experiments were conducted on a system from Mettler Toledo (TGA/SDTA 851 model). The experiments were conducted in air flow at the rate of 50 mL/min, with a temperature increase from 20° to 1000°C at a rate of 5 °C·min^{-1}.

Hydrogen chemisorption was conducted at 40 °C using a Micromeritics Autochem II 2920 apparatus. The calcined samples (0.05 g) were introduced into a quartz U-shaped tube reactor and reduced for 1 h at 300 °C (5 °C·min^{-1} heating rate) under a flow of hydrogen (50 mL·min^{-1}) to fully reduce the platinum, then purged with argon (50 mL·min^{-1}) at the same temperature and duration. The reactor was cooled down to the adsorption temperature (40 °C) using argon, and the measurements were undertaken through pulse injections (0.551 mL) of 10%H_2/Ar until saturation. Hydrogen consumption was monitored using a thermal conductivity detector (TCD).

2.4. Catalytic tests

Formaldehyde oxidation tests were performed in a fixed bed reactor (internal diameter = 10 mm) loaded with the catalyst (0.025 g, 40–60 mesh, diluted by 1.2 g SiC). In some tests, 0.05 g catalyst diluted by 2.4 g SiC or 0.1 g catalyst diluted by 4.8 g SiC was used. Before each light-off test, the catalyst was pretreated at 100 °C for 1 h under O_2/N_2 flow (20 vol%, 100 mL min^{-1}) to remove water and surface impurities. Gaseous HCHO was generated from para-HCHO in a permeation tube placed in a permeation chamber (Dynacalibrator, VICI Metronics Inc.). By adjusting the gas carrier flow (O_2 (20 vol%)/N_2) rate and the chamber temperature, a stable HCHO concentration was generated. The inlet concentration of HCHO was fixed at 100 ppm$_v$, and the total flow rate was 100 mL·min^{-1}. After pre-treatment, the reactive flow was flushed over the catalyst at 100 °C for another 1 h and the temperature was then allowed to decrease from 100° to 25°C at a ramp of 0.2 °C·min^{-1}. In the humidity tests, the temperature was directly maintained at 40 °C for 1 h for each humidity (dry air, 25%, 50% and 75%). In dry air, no additional water was introduced except for the trace content of water in the original gas bottle of air and N_2. The outlet gas was monitored online using a gas chromatograph (Varian) equipped with a thermal conductivity detector. Separations were performed using two columns: one CP-Sil 5 CB column channel (8 m) for HCHO analysis, and one CO_x column channel (1 m) for CO_2 analysis. X_{CO2} (Eq. S8) represents the oxidation of HCHO into CO_2, while HCHO elimination or total removal of HCHO is given by X_{HCHO} (Eq. S9). Carbon balance was deduced based on Eq. (S13), knowing that no CO was detected when using GC-MS detection. Turnover frequency (*TOF*, s^{-1}) and reaction rate (*r*, mol·s^{-1}·g_{Pt}^{-1}) was deduced based on Eqs. (S10 and S11), respectively. Activation energies (E_a, J·mol^{-1}) were calculated using the Arrhenius relationship (Eq. S12).

2.5. Adsorption tests

Formaldehyde adsorption tests were performed in the same fixed bed reactor as for formaldehyde oxidation tests loaded with the SiO$_2$-x samples pretreated under vacuum for 3 h at 150 °C. The inlet concentration of HCHO was set at 3 ppmv, and GHSV was 33,600 mL·g^{-1}·h^{-1}. The atmosphere used in the adsorption tests were dry air and air with 25% humidity, respectively, for each SiO$_2$-x sample.

3. Results and discussion

3.1. Support characterization

The surface OH content of the different SiO_2 samples was examined via different characterization techniques. XPS was used to detect the different surface oxygen species. Fig. 1a and Fig. S1 show the high-resolution O 1 s and Si 2p XPS spectra of the different SiO_2 samples, respectively. Firstly, the peak decomposition of O 1 s spectra has demonstrated three peaks located at 532.8, 533.3, and 535.1 eV, corresponding to O^{2-}, OH, and adsorbed H_2O, respectively [26]. Relative amounts of OH groups were estimated to 29.7%, 23.1%, and 20.6% for SiO$_2$-4.5, SiO$_2$-3.1 and SiO$_2$-2.3, respectively, which indicates a gradual decrease of the surface OH density of the silica support due to the replacement of Si-OH with O-Si(CH$_3$)$_3$ during the silylation reaction with the increased quantity of HMDS. Secondly, in contrast to SiO$_2$-4.5, the peak decomposition of Si 2p spectra of both SiO$_2$-2.3 and SiO$_2$-3.1 exhibited two contribution peaks at around 103.8 and 101.8 eV, indexing to Si-O-Si and O-Si(CH$_3$)$_3$, respectively, [27], indicating the successful replacement of hydroxyls with O-Si(CH$_3$)$_3$ on SiO$_2$-2.3 and SiO$_2$-3.1 surface.

The surface functional groups of the SiO$_2$ samples were further identified by FT-IR as depicted in Fig. 1b. For non-passivated SiO$_2$-4.5, the broad peak band at 3200–3600 cm^{-1} is assigned to the asymmetric stretching vibrations of O-H bonds in –OH groups bonded on the particle surface, and the absorption peak at 1636 cm^{-1} represents bending vibrations of O-H bonds. The characteristic bands at 1091 and 803 cm^{-1} correspond to asymmetric and symmetric stretching vibrations of Si-O-Si, respectively [28]. By contrast with SiO$_2$-4.5 spectrum, SiO$_2$-2.3 and SiO$_2$-3.1 spectra clearly show two new absorption bands at 2965 and 2820 cm^{-1} which are assigned to the asymmetric and symmetric stretching vibration of the C-H bonds in –CH$_3$ groups united on the SiO$_2$ surface, respectively [29], implying the successful grafting of –CH$_3$ groups from HMDS on SiO$_2$ surface.

Densities of OH groups in SiO$_2$ samples were quantified via TG analysis while their surface carbon contents were measured through CHN analysis. The TG curves obtained in air atmosphere of the SiO$_2$ samples were shown in Fig. 1c. All of the SiO$_2$ samples exhibit three sequential stages, the first stage occurs between 30 °C and 200 °C due to the elimination of physically adsorbed water. At this stage, SiO$_2$-x can be classified in the following order for weight loss: SiO$_2$-4.5 > SiO$_2$-3.1 > SiO$_2$-2.3, indicating that the surface grafting of the -(CH$_3$)$_3$ groups enhances the surface hydrophobicity of SiO$_2$. The second stage ranges from 200° to 800°C which can be attributed to the decomposition of the surface groups: for SiO$_2$-4.5, the surface evolution primarily involves the dehydroxylation condensation reaction of various silanols including isolated, geminal and vicinal silanols; for SiO$_2$-2.3 and SiO$_2$-3.1, the thermal degradation of both silanol and trimethylsilyl functional groups contributes to the total weight loss [29]. The OH density of each sample was evaluated through the weight loss determination at this stage, where the weight ratio of the -(CH$_3$)$_3$ groups was also considered in the cases of SiO$_2$-2.3 and SiO$_2$-3.1 (see the calculation details in supporting information). As summarized in Table 1, SiO$_2$-4.5, SiO$_2$-3.1 and SiO$_2$-2.3 samples display an OH density of 4.5, 3.1 and 2.3 OH nm^{-2}, respectively. In addition, at the third stage from 800° to 1000°C a negligible weight loss is observed for all the samples, which could be assigned to the further reduction of the buried silanol groups in bulk [30]. According to the CHN analysis, the carbon content of SiO$_2$-2.3 and SiO$_2$-3.1 (Table 1) is 3.2% and 2.1%, respectively, which correspond to a -(CH$_3$)$_3$ density of 2.3 and 1.5 -(CH$_3$)$_3$ nm^{-2}, respectively. Based on the method used in this work to prepare SiO$_2$-2.3 and SiO$_2$-3.1 from SiO$_2$-4.5, the sum of OH density and -(CH$_3$)$_3$ density equals to 4.5 nm^{-2}. Therefore, for SiO$_2$-2.3 and SiO$_2$-3.1, OH densities of 2.2 and 3.0 OH nm^{-2}, respectively, can be deduced from CHN analysis, which is very close values derived from TG analysis.

Based on the above described quantitative analysis, it is necessary to
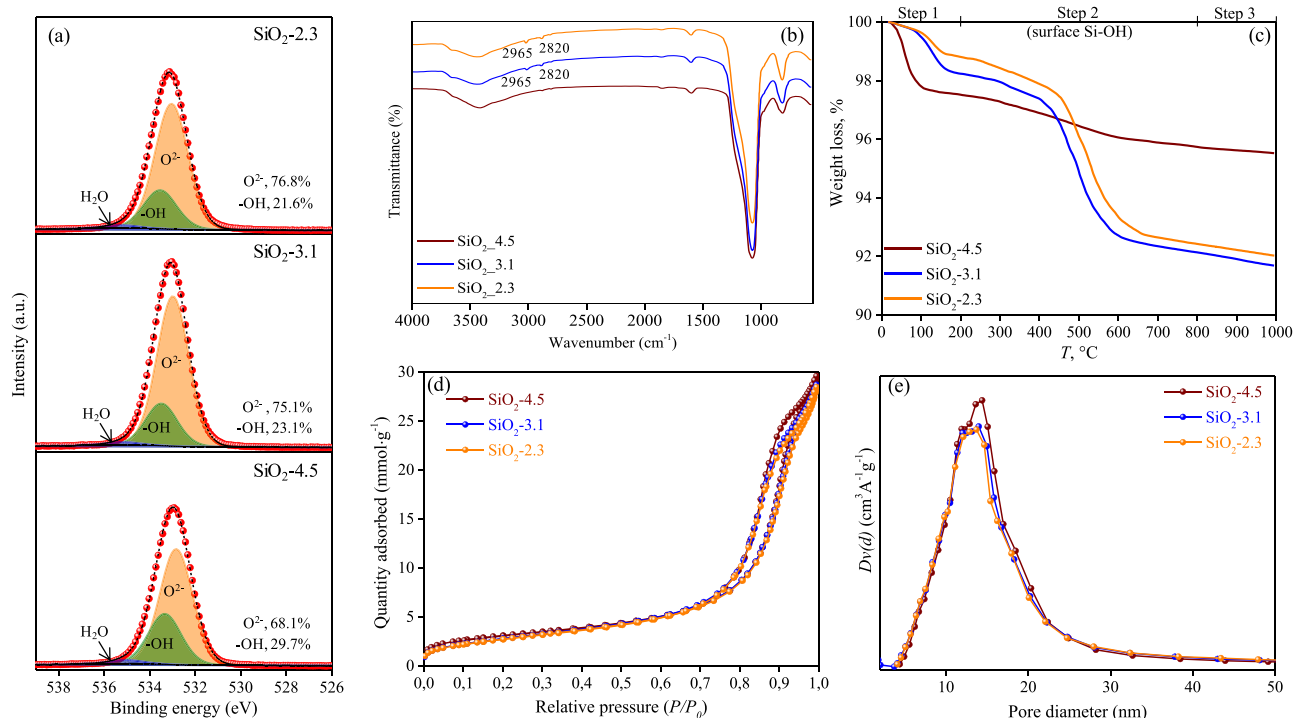
Fig. 1. (a) High-resolution O 1 s XPS spectra; (b) FT-IR spectra; (c) TG curves in air atmosphere; (d) N_2 physisorption isotherms and (e) BJH pore size distribution (based on the desorption branch of the isotherm) for SiO_2-x samples (x = 2.3, 3.1, 4.5).

Table 1
Properties of SiO_2 supports.

Samples	S_{BET},[a] $m^2 \cdot g^{-1}$	V_p,[b] $cm^3 \cdot g^{-1}$	D_p,[c] nm	$w (T_{200})$,[d] wt%	$w (T_{800})$,[e] wt%	w (C),[f] wt%	d (OH),[g] OH nm^{-2}	d (OH),[h] OH nm^{-2}
SiO_2-4.5	257	1.07	14.4	97.5	95.8	-	4.5	-
SiO_2-3.1	239	1.03	14.0	98.2	92.1	3.2	3.1	3.0
SiO_2-2.3	233	1.02	13.7	98.8	92.4	2.1	2.3	2.2

[a] S_{BET}, surface area per gram of SiO_2 support. [b] Total pore volume per gram of SiO_2 support estimated from the nitrogen adsorbed at P/P_0 = 0.99. [c] BJH mean pore size. [d] Weight percentage in TG analysis at 200 °C. [e] Weight percentage in TG analysis at 800 °C. [f] Carbon content deduced from CHN analysis. [g] d(OH), density of OH groups desorbed in the temperature range from 200° to 800°C in accordance with TG data and calculated by Eq. S1 and Eq. S2. [h] OH density obtained based on CHN analysis and TG analysis.

indicate that there appears a limit for the silylation reaction between Si-OH and HMDS to consume the surface Si-OH groups: though a theoretical amount of HMDS to consume the total surface OH groups of SiO_2-4.5 was applied to prepare SiO_2-2.3, the final surface OH density was not as low as expected but remained around 2.3 OH nm^{-2}. In fact, the surface reaction between HMDS and surface OH groups is self-limiting, and the OH groups are only replaced as long as new -O-Si(CH₃)₃ groups can still be accommodated on the surface [31]. The maximum density of the -O-Si(CH₃)₃ groups on silica surface was calculated as shown in Supporting Information. A steric limit of 2.4 -O-Si(CH₃)₃ nm^{-2} was obtained, which corresponds to a surface OH density of 2.1 OH nm^{-2} at the end of surface silylation reaction. This value is close to the value obtained via TG (2.3 OH nm^{-2}) and CHN (2.2 OH nm^{-2}) analysis.

Textual properties of the different silica support were investigated by N_2-physisorption, as presented in Fig. 1d and 1e and Table 1. Isotherms of SiO_2-2.3, SiO_2-3.1 and SiO_2-4.5 are of Type IV with H2 type-like hysteresis according to the IUPAC classification, which are characteristic of the mesoporous materials [32]. As compared to SiO_2-4.5 (257 $m^2 \cdot g^{-1}$), only a slight decrease (∼ 7%) in the specific surface area could be observed for SiO_2-3.1 (239 $m^2 \cdot g^{-1}$) and SiO_2-2.3 (233 $m^2 \cdot g^{-1}$). Limited changes are also observed for the pore volume and the average pore diameter (Table 1). Therefore, surface passivation had negligible effects on materials textural characteristics.

3.2. Catalyst characterization

During catalyst preparation, owing to the thermal treatments and the interaction between Pt NPs and silanols, the surface OH content of the final $PtSiO_2$-x will be inevitably affected. The surface OH content on different Pt/SiO_2 samples was quantified by TG analysis. The TG curves of Pt/SiO_2 samples obtained in air atmosphere, as presented in Fig. S12, are similar to those of SiO_2-x. The $PtSiO_2$-x samples also exhibit three sequential stages, the second stage ranging from 200° to 800°C being dedicated to surface groups decomposition. The surface evolution of $PtSiO_2$-4.5 primarily involves the dehydroxylation condensation reaction of various silanols. The thermal degradation of both silanol and trimethylsilyl functional groups are involved for $PtSiO_2$-2.3 and $PtSiO_2$-3.1. As summarized in Table 2, $PtSiO_2$-4.5, $PtSiO_2$-3.1 and $PtSiO_2$-2.3 display a surface silanol density of 3.4, 2.0 and 1.1 OH nm^{-2}, respectively. As compared to their corresponding SiO_2 supports, there is a decrease in surface OH content in Pt/SiO_2, which could primarily be assigned to the thermal treatments (350 °C for 6 h in air and 300 °C for 2 h in H_2) during the catalyst preparation process, considering that the silanol content start to decrease at 200 °C. The interaction between Pt NPs and surface silanols of SiO_2 may also contribute in a minor way. The thermal treatments hardly affect the content of the surface O-Si(CH₃)₃ which generally decompose at 400 – 700 °C in air [33].

SiO_2 with controlled surface OH densities was then used as support to

Table 2

Textural and structural properties of the synthesized samples.

Samples	x_{Pt}, wt%	S_{BET},[a] m²/g	V_p,[b] cm³/g	D_p,[c] nm	D_H,[d] %	d (OH),[e] OH nm⁻²	particle size, nm	
							d_H,[f] nm	d_{Pt},[g] nm
PtSiO₂-4.5	0.19	246	1.03	14.3	81.2	3.4	1.02	1.05
PtSiO₂-3.1	0.19	235	1.00	13.3	78.5	2.0	1.09	1.10
PtSiO₂-2.3	0.21	232	0.99	12.2	78.1	1.1	1.10	1.12

[a] S_{BET}, surface area per gram of SBA-15 support. [b] Total pore volume per gram of SBA-15 support. [c] D_p, BJH mean pore size. [d] D_H, Pt dispersion deduced from hydrogen chemisorption via Eq. S5. [e] $d(OH)$, density of OH groups desorbed in the temperature range from 200° to 800°C in accordance with TG data and calculated with Eq. S1 and Eq. S2. [f] d_H, Pt particle size deduced from hydrogen chemisorption via Eq. S6. [g] d_{Pt}, Pt particle size determined by HAADF-STEM measurement.

prepare Pt/SiO₂ catalysts (PtSiO₂-*x*, *x* = 2.3, 3.1, 4.5). For ensuring the production of PtSiO₂-*x* bearing Pt NPs of similar physiochemical properties, Pt NPs with controlled particle size were fabricated beforehand by the ethylene glycol reduction method. Fig. S2 presents the size distribution of the as-prepared Pt NPs deduced from the DLS analysis, which indicates a relatively uniform size distribution with an average particle size of 1.1 nm. The PtSiO₂-x samples were prepared via wet impregnation and went through the same thermal treatments. HAADF-

STEM, XRD, hydrogen chemisorption, XPS and N₂ physisorption are used to analyse the nanoscale structure of catalysts. All the characteristics of the studied samples are summarized in Table 2.

Fig. S3 shows XRD patterns of the SiO₂ support and the reduced Pt/SiO₂ samples. Diffraction peaks characteristic to metallic platinum could not be observed whatever the SiO₂ support, suggesting that the small size of the highly dispersed Pt NPs in these Pt/SiO₂ samples was beyond the detection limit of the XRD apparatus.
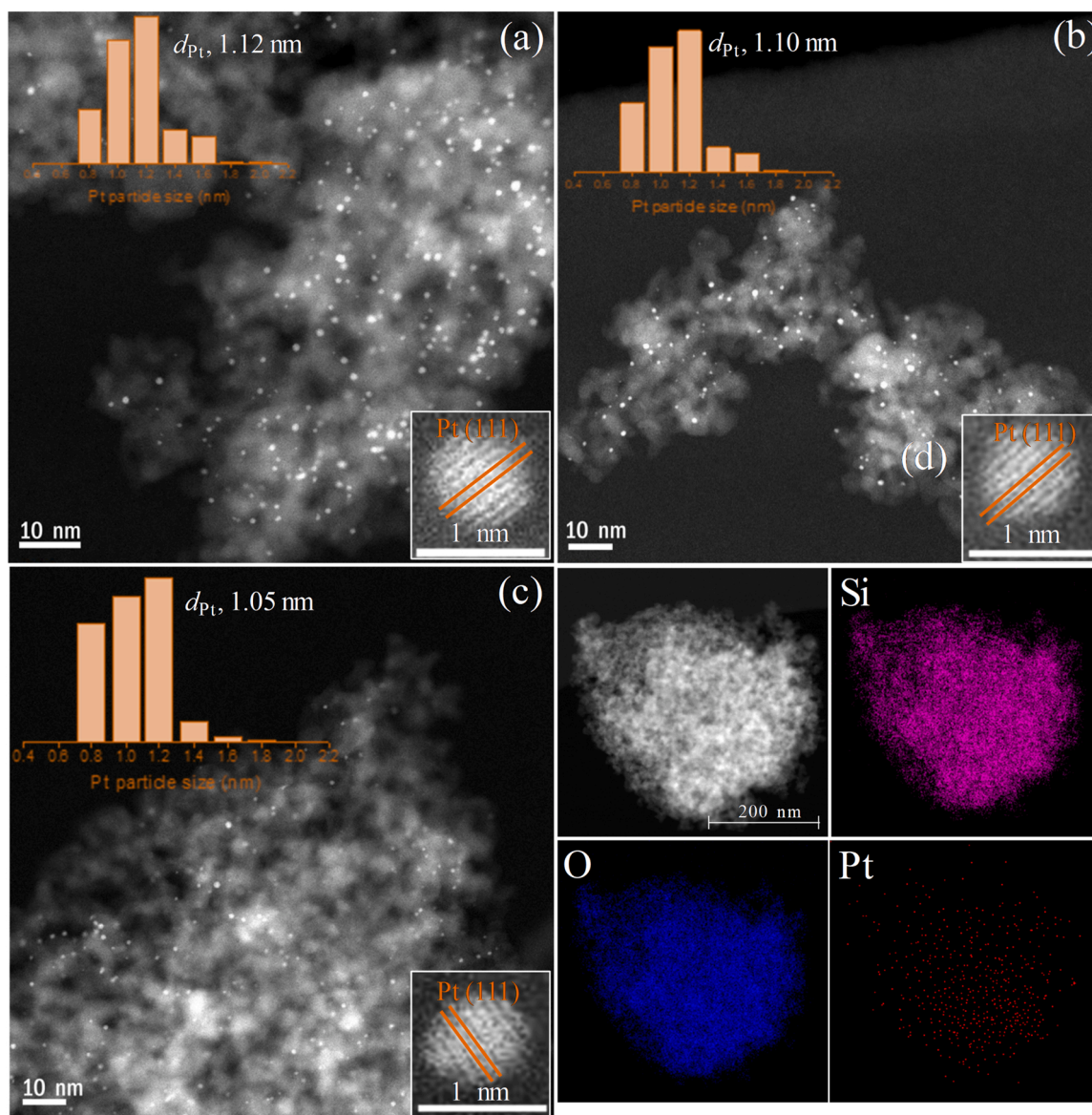
Fig. 2. HAADF-STEM images and size distributions of the H₂-reduced catalysts: (a) PtSiO₂-2.3; (b) PtSiO₂-3.1; (c) PtSiO₂-4.5; (d) EDS element mapping of Si, O and Pt in PtSiO₂-4.5.

The fine dispersion of Pt particles on SiO_2 was confirmed by microscopy images. Fig. 2, S4 and S5 show HADDF-STEM images and size distributions of the reduced $PtSiO_2$-x samples. It could be observed that whatever the support, Pt/SiO_2 exhibits extremely tiny nanoparticles that are uniformly dispersed on SiO_2 surface, as well as similar particle size distribution centered at around 1.1 nm. One of the spots was randomly selected to analyse the fringe patterns and the corresponding high-magnification STEM images show the lattice fringes with interplanar distances of 0.23 nm, which is in good agreement with the (111) plane of metallic Pt [34]. Accordingly, these nanoparticles are confirmed to be the Pt particles. All these results show that their size distribution remained unchanged after the catalyst impregnation process, which is in agreement with the previous report [35]. Besides, the particle diameters (see in Table 2) determined from H_2 chemisorption are in the same range as those deduced from the microscopy analysis. Moreover, Pt metal dispersions of $PtSiO_2$-4.5, $PtSiO_2$-3.1 and $PtSiO_2$-2.3 are 88.6%, 86.7% and 84.8%, respectively. These results indicate that the different surface silanol content of the SiO_2 support led only to a negligible difference in the final Pt dispersion on SiO_2.

XPS analysis of the reduced $PtSiO_2$-x samples was used to probe the valent state of Pt, which is summarized in Fig. 3. It could be observed that whatever the support, the three Pt/SiO_2 samples present Pt 4 f peaks at very close positions: $PtSiO_2$-3.1 and $PtSiO_2$-4.5 give Pt 4f7/2 at 71.6 eV and Pt 4f5/2 at 74.9 eV while $PtSiO_2$-2.3 gives Pt 4f7/2 at 71.4 eV and Pt 4f5/2 at 74.7 eV. These peak positions are in good agreement with values reported for metallic Pt [36], which is consistent with the microscopy analysis result. The $PtSiO_2$-x samples also exhibit

Fig. 3. XPS spectra of Pt 4 f electrons of hydrogen reduced Pt/SiO_2 samples: (a) $PtSiO_2$-4.5 (b) $PtSiO_2$-3.1 (c) $PtSiO_2$-2.3.

very close porosity properties, as revealed by the N_2 physisorption analysis as summarized in Fig. S6 and Table 2. All of the three $PtSiO_2$ samples inherit the isotherms of the corresponding SiO_2 support: type IV with H2 type-like hysteresis. Whatever the support, Pt loading on SiO_2 led to only a tiny decrease in the specific surface area and pore volume, after introduction of Pt particles into the support porosity.

3.3. Formaldehyde oxidation performance

The catalytic performance of the various Pt/SiO_2 catalysts was evaluated in HCHO oxidation as shown in Fig. 4a. Due to the catalyst activity, in order to highlight the difference of the catalytic performance of the Pt/SiO_2 catalysts, the GHSV was adjusted to 240,000 mL·g^{-1}·h^{-1} (catalyst mass, 25 mg) in each test. It was observed that under the dry air conditions, $PtSiO_2$-2.3 showed only 2% of HCHO conversion at 30 °C. $PtSiO_2$-3.1 exhibited a similar catalytic performance in low temperature range though it showed a relatively higher catalytic activity than $PtSiO_2$-2.3 at high temperature. In contrast, $PtSiO_2$-4.5 demonstrated a significantly enhanced performance with a HCHO conversion into CO_2 (X_{CO2}) reaching 39% at 30 °C. The $T_{50\%}$ (temperature at which 50% HCHO conversion reached) for $PtSiO_2$-2.3, $PtSiO_2$-3.1 and $PtSiO_2$-4.5 is 100 °C, 88 °C and 40 °C, respectively. Accordingly, considering their activities in dry environment, the three catalysts can be classified as follows: $PtSiO_2$-4.5 > > $PtSiO_2$-3.1 > $PtSiO_2$-2.3. In addition, the carbon balance on each $PtSiO_2$-x sample was deduced as shown in Fig. S13, which indicates a negligible carbon deposition phenomenon with Pt/SiO_2 catalysts.

Based on the overall structural analysis as discussed in Sections 3.1 and 3.2, $PtSiO_2$-2.3, $PtSiO_2$-3.1 and $PtSiO_2$-4.5 have similar porosity properties, Pt particle morphology (size and shape) and Pt valent state in close proximity to each other. Hence, the different activity of Pt/SiO_2 in HCHO oxidation could be attributed to the dominant influence of the discrepancy between the silanol densities of these Pt/SiO_2 catalysts. Notably, when the GHSV of $PtSiO_2$-4.5 was decreased to 60,000 mL·g^{-1}·h^{-1} (catalyst mass, 100 mg), which is a common quantity usually used in literature, a full HCHO conversion into CO_2 at room temperature is observed, and the catalyst could continuously be efficient for over 48 h without obvious reactivity loss, as presented in Fig. 4b, which makes $PtSiO_2$-4.5 one of the most reactive and stable noble metal catalysts reported in the literature [2,15,16].

To further investigate the effect of the hydroxyl groups on the HCHO decomposition activity in indoor environment, the catalytic performance of the various Pt/SiO_2 catalysts was further tested under various humidity conditions at 40 °C. Fig. 4c presents HCHO conversion versus reaction time at 40 °C. In dry environment, the reaction rate of $PtSiO_2$-4.5 is 61.4 μmol·s^{-1}·g$_{Pt}^{-1}$, which is 1.9 times and 3.9 times higher than that of $PtSiO_2$-3.1 (32.6 μmol·s^{-1}·g$_{Pt}^{-1}$) and $PtSiO_2$-2.3 (15.7 μmol·s^{-1}·g$_{Pt}^{-1}$), respectively. Apparently, Pt/SiO_2 with a high silanol density possesses an excellent performance at low temperature, in consistent with the light-off tests as discussed above. When the relative humidity of feed gas was increased to 25%, HCHO conversions (Fig. 4c), reaction rates (Fig. 4d) and *TOFs* (Table S1) of three catalysts were all evidently raised. For instance, reaction rates with $PtSiO_2$-2.3, $PtSiO_2$-3.1 and $PtSiO_2$-4.5 have remarkably increased 3.4 times, 2.2 times and 1.3 times, respectively, demonstrating a promoting role of the external water in HCHO oxidation, which is, for the first time, observed with the SiO_2 supported noble metal catalysts. With further increasing the relative humidity from 25% to 50%, and up to 75%, the HCHO oxidation rate of $PtSiO_2$-2.3 was slowly increased, the HCHO oxidation rate of $PtSiO_2$-3.1 basically remained stable while the reaction rate of $PtSiO_2$-4.5 was slightly suppressed. At 75% relative humidity, the reactivity gap between $PtSiO_2$-2.3 and $PtSiO_2$-3.1 and $PtSiO_2$-4.5 was obviously narrowed. The different reactivity exhibited by Pt/SiO_2 with different silanol density under a given humidity condition indicates an important effect of interactions between water molecules and Si-OH groups of SiO_2 on the oxidative decomposition of HCHO on Pt active sites.
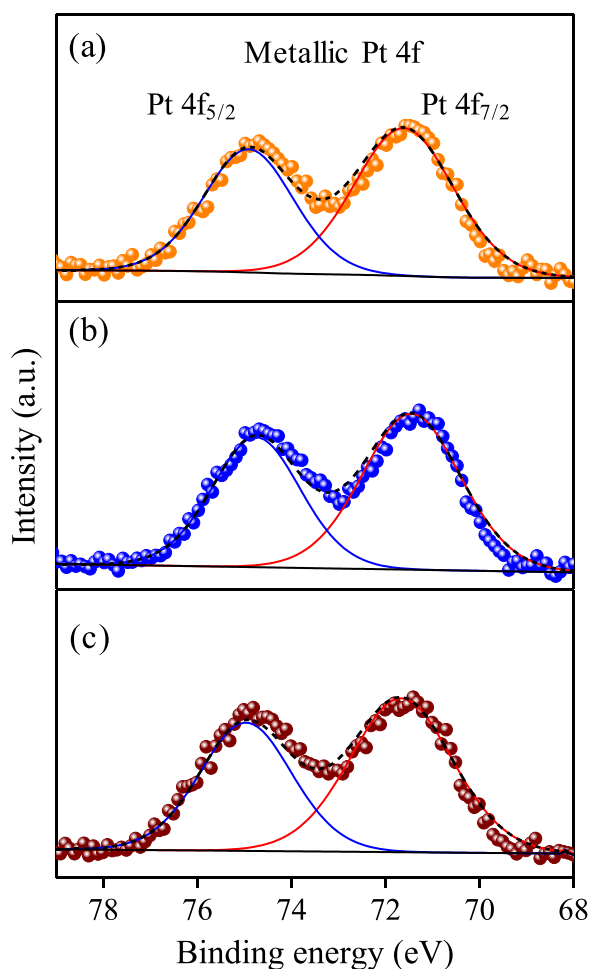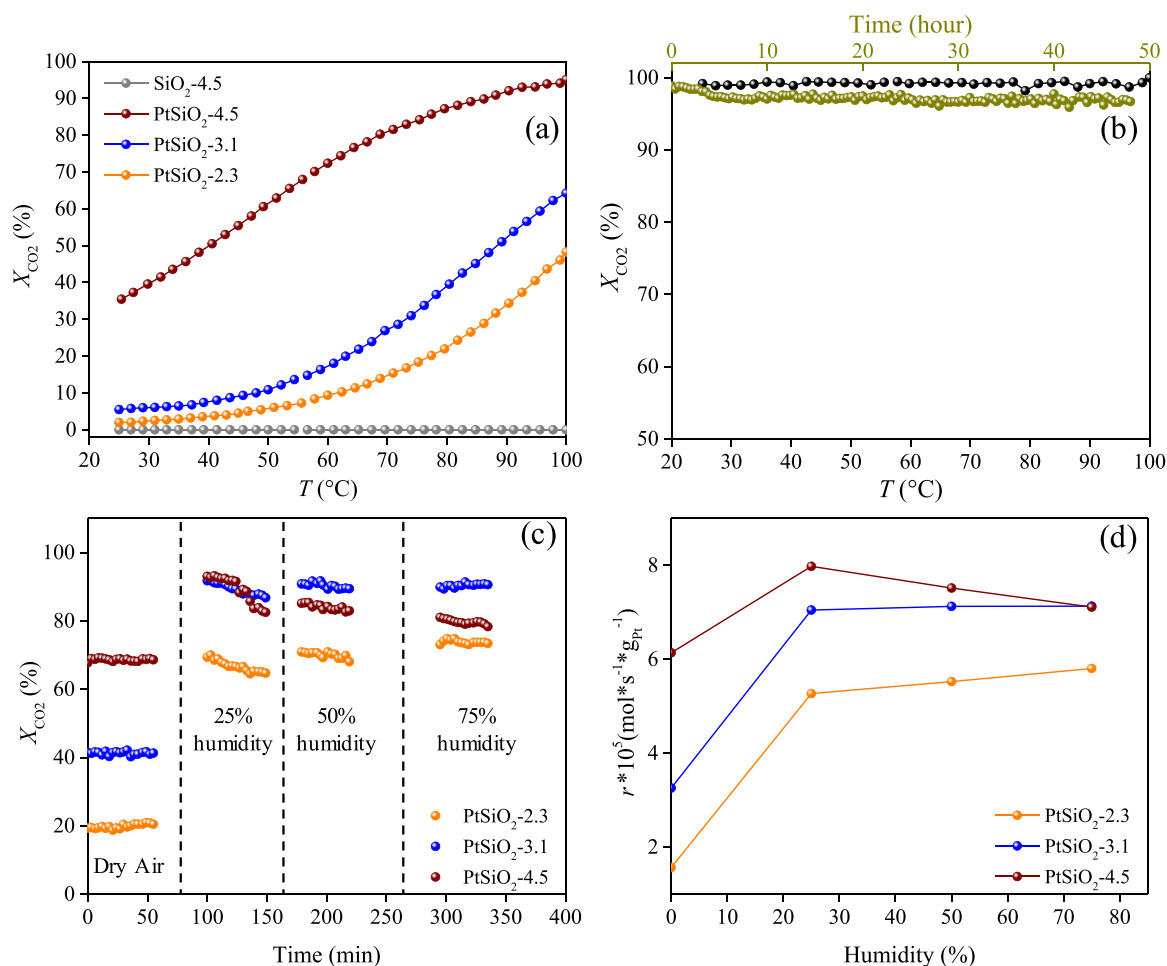
Fig. 4. (a) HCHO conversion into CO_2 (X_{CO_2}) as a function of reaction temperature (100 ppm HCHO, GHSV = 240,000 mL·g^{-1}·h^{-1}); (b) HCHO conversion as a function of reaction temperature and time over PtSiO$_2$-4.5 (100 ppm HCHO, GHSV = 60,000 mL·g^{-1}·h^{-1}); (c) HCHO conversion as a function of reaction time under different humidity conditions (100 ppm HCHO, GHSV = 120,000 mL·g^{-1}·h^{-1}, Reaction temperature = 40 °C); (d) and the corresponding reaction rate as a function of relative humidity for the various catalysts.

Kinetic measurements were performed to compare intrinsic activities of the various Pt/SiO$_2$-x catalysts. Fig. S7 displays Arrhenius plots used for determining the catalysts apparent activation energies. For PtSiO$_2$-4.5, the apparent activation energy is 21.9 kJ/mol, which is obviously lower than for PtSiO$_2$-2.3 (40.7 kJ/mol) and PtSiO$_2$-3.1 (31.0 kJ/mol). This confirms that Pt/SiO$_2$ with higher surface Si-OH density is

intrinsically more active in HCHO oxidation, probably resulting from the fact that the OH-rich catalyst provides a surface environment that facilitates the HCHO adsorption and oxidative decomposition [22].
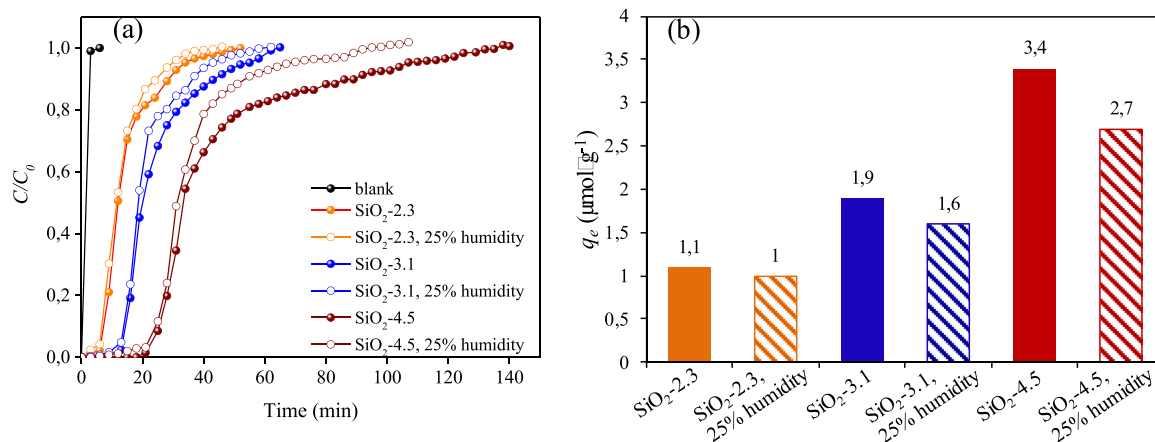
Fig. 5. (a) HCHO breakthrough profiles over SiO$_2$-2.3, SiO$_2$-3.1 and SiO$_2$-4.5 under dry and humidity conditions (25 °C, atmospheric pressure, 3 ppm$_v$ of inlet HCHO concentration, GHSV 33,600 mL·g^{-1}·h^{-1}); (b) Adsorption capacity of HCHO estimated from breakthrough profiles.

3.4. Mechanism study

3.4.1. Effect of silanol density on formaldehyde adsorption

The above presented catalytic results have revealed an important influence of surface silanol groups at the surface of Pt/SiO$_2$ in HCHO oxidation. For clarifying the mechanism behind the role of Si-OH groups in HCHO oxidation, a series of fixed-bed dynamic adsorption experiments was performed to identify the effect of the surface OH density on the HCHO adsorption capacity of the SiO$_2$ adsorbents. As presented in Fig. 5, the shape of the obtained breakthrough curves is rather similar in all cases: after the breakthrough point (10% of the inlet HCHO concentration penetrating the adsorbent bed), a sharp increase in the outlet concentration (implying a fast adsorption kinetic) followed with a "tailing" of the breakthrough curve (a slow approach of C/C_0 (the ratio of the outlet HCHO concentration (C) versus the initial HCHO concentration (C_0)) towards 1, usually caused by the dominant mass transfer process) [37]. Under the dry air condition, the HCHO breakthrough times, saturation times and dynamic adsorption capacities increased with the surface OH density of SiO$_2$ as follows: SiO$_2$-2.3 < SiO$_2$-3.1 < SiO$_2$-4.5 (See in Table 3), suggesting a promoting effect of the surface silanol groups in SiO$_2$ on HCHO adsorption. In fact, surface silanols on silica are presumed to be hydrogen-bonded with the carbonyl function of the HCHO molecule through the oxygen long pair, thus promoting their adsorption [38]. Besides, for eliminating the possible influence of the subtle porosity difference between the SiO$_2$ adsorbents, which may also slightly affect the adsorption performance, the C/C_0 ratio in the breakthrough profiles was further normalized by the S$_{BET}$ difference (Fig. S8). After normalization, the same trend of HCHO adsorption capacity with silanol density has remained similar, implying the negligible effect of the porosity difference on the adsorption capacity of the studied SiO$_2$ samples.

Under the humidity condition, an inhibitory effect of water on HCHO adsorption was observed: the introduction of 25% humidity in the gas feed led to a decrease in the HCHO breakthrough times, saturation times and dynamic adsorption capacities in all cases when comparing to the corresponding dry adsorption conditions (See in Fig. 5 and Table 3). In detail, the resulting decrease in adsorption capacity is − 9.1%, − 16% and − 21% for SiO$_2$-2.3, SiO$_2$-3.1, and SiO$_2$-4.5, respectively, indicating an especially more pronounced inhibitory effect of water on SiO$_2$ adsorbent with a higher silanol density. The main mechanisms behind the drop of the adsorption capacity of SiO$_2$ under the humidity condition are possibly related to: (i) competitive adsorption between water and HCHO on the same active surface sites; (ii) blockage of pores and surface sites by the adsorbed moisture at high humidity condition [39].

3.4.2. Molecular description of the adsorption of involved reactants from DFT calculations

HCHO oxidation reaction involves HCHO, O$_2$, H$_2$O, CO$_2$ as reactants/products, and CO as a potential intermediate product. For elucidating the mechanism behind the gas adsorption and HCHO decomposition in different surface environment, we studied the interaction between these molecules and the various pure silica or Pt/SiO$_2$ surfaces by means of DFT calculations.

3.4.2.1. Adsorption on various pure SiO$_2$ surfaces.

SiO$_2$ surfaces with a wide range of silanol density equal to 1.1, 2.0, 3.3, 4.6, 5.9 and 7.2 OH·nm^{-2}, respectively (denoted as silica-1.1, silica-2.0, silica-3.3, silica-4.6, silica-5.9, and silica-7.2) were modelled via dehydroxylation of a fully hydroxylated surface. These amorphous models have been successfully used in adsorption and catalytic studies [40,41]. The geometrical structures of the considered amorphous silica surfaces are presented in Fig. S9. In order to find the most stable structures of the adsorbed molecule (HCHO, CO$_2$, O$_2$, H$_2$O and CO) onto amorphous silica surfaces with various silanol density, different geometrical configurations have been investigated at various adsorption sites (geminal, vicinal, isolated, nest-1 and nest-2, illustrated in Fig. S10). Two interaction modes via hydrogen bond have been evidenced for HCHO: the perpendicular O-interaction (denoted perp O-int) through oxygen atom with the silanol group, and the flat O-interaction (denoted flat O-int) through oxygen atom, carbon and hydrogen atoms. The most stable interaction structures for HCHO on various SiO$_2$ surfaces are presented in Fig. S11.

The computed adsorption energy of HCHO, CO$_2$, O$_2$, H$_2$O and CO molecules over different pure silica surfaces at different adsorption sites are gathered in Table S2. On SiO$_2$-1.1 surface, there are only isolated silanols [42], and the adsorption energy (ΔE) of HCHO and H$_2$O are around − 30 kJ·mol^{-1}, − 13 kJ·mol^{-1} for CO$_2$ and CO, and − 5 kJ·mol^{-1} for O$_2$. On SiO$_2$-2.0 surface, HCHO prefers to adsorb on nest-1 via flat O-int with ΔE of − 37 kJ·mol^{-1}, while CO$_2$ is adsorbed on vicinal with ΔE of − 19 kJ·mol^{-1}. O$_2$ and H$_2$O tend to adsorb on nest-1 with ΔE of − 8 and − 55 kJ·mol^{-1}, respectively, while CO is adsorbed on the isolated site with ΔE of − 14 kJ·mol^{-1}. For SiO$_2$-3.3, all molecules are apt to accommodate on the nest-2 site with ΔE of − 54, − 22, − 10, − 70, and − 12 kJ·mol^{-1} for HCHO, CO$_2$, O$_2$, H$_2$O, and CO molecules, respectively. On SiO$_2$-4.6 surface, HCHO prefers to adsorb on nest-1 and nest-2 via flat and perp O-int modes, respectively, with the same ΔE of − 52 kJ·mol^{-1}. CO$_2$, O$_2$, H$_2$O, and CO tend to occupy the vicinal, nest-2, nest-1, and nest-2 silanol sites with ΔE of − 27, − 11, − 81, and − 21 kJ·mol^{-1}, respectively. On SiO$_2$-5.9, HCHO inclines to accommodate on nest-2 via both perp and flat O-int modes ($\Delta E \approx$ −63 kJ·mol^{-1}). CO$_2$ and O$_2$ also prefer to occupy the nest-2 site with ΔE of − 27 and − 13 kJ·mol^{-1}, respectively. However, H$_2$O is strongly adsorbed on the isolated site with ΔE of − 76 kJ·mol^{-1}. CO could coexist on nest-1 and nest-2 with the same energy value of − 14 kJ·mol^{-1}. On SiO$_2$-7.2, the favoured adsorption sites of HCHO, CO$_2$, and O$_2$ are similar to those on SiO$_2$-5.9 with a slight increase in the corresponding ΔE by about 10 kJ·mol^{-1} mainly due to the increased silanol density. CO prefers to accommodate on both vicinal and nest-2 with the same ΔE of − 21 kJ·mol^{-1}. As summarized in Fig. 6a, it could be clearly observed that the adsorption energy of the considered molecules increases mainly as a function of the silanol density of the silica surface. The aforementioned adsorption test results have revealed that the silanol-rich SiO$_2$ surface benefits the HCHO adsorption. This is consistent with the computing results here. Moreover, the inhibitory effect of CO$_2$, O$_2$, and CO on HCHO adsorption is negligible, while the adsorption energies of H$_2$O are slightly larger than those of HCHO, which suggests that H$_2$O acts as a major inhibitor for HCHO adsorption on pure silica surface whatever the silanol density. This explains why under humid conditions
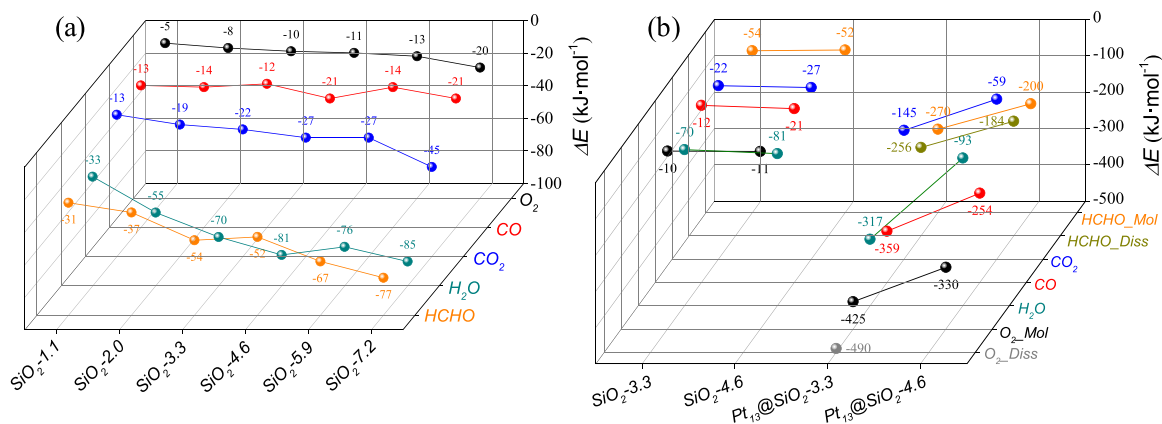
Table 3

Comparison of stoichiometric time and dynamic adsorption capacity of HCHO for all SiO$_2$ adsorbents under dry and wet conditions.

Samples	SiO$_2$-2.3			SiO$_2$-3.1		SiO$_2$-4.5	
	dry air		25% humidity	dry air	25% humidity	dry air	25% humidity
t_b (min)[a]	7.2		6.6	14.4	13.9	25.4	24.2
t_s (min)[b]	28.6		24.5	43.6	36.4	89.6	53.6
q_e (µmol·g^{-1})[c]	1.1		1.0	1.9	1.6	3.4	2.7

[a] t_b: breakthrough time, when 10% of the inlet HCHO concentration penetrated the adsorbent bed. [b] t_s: saturation time, when 90% of the inlet HCHO concentration left the adsorbent bed. [c] q_e: HCHO adsorption capacity of different SiO$_2$ adsorbents estimated from the breakthrough profiles based on Equation S7 (25 °C, atmospheric pressure, 3 ppm$_v$ of inlet HCHO concentration, GHSV 33,600 mL·g^{-1}·h^{-1}).

Fig. 6. PBE+D2 calculated adsorption energy of the most stable configuration of HCHO, H_2O, CO, CO_2 and O_2 on (a) amorphous silica surfaces with different silanol density; (b) on representative supported Pt@SiO$_2$ and corresponding pure silica surfaces. HCHO_Mol: HCHO molecule; HCHO_Diss: dissociated HCHO species; O$_2$_Mol: O_2 molecule; O$_2$_Diss: dissociated O_2 species.

the adsorption capacity of the tested SiO$_2$ samples decreased.

3.4.2.2. Adsorption on various Pt/SiO$_2$ catalyst surfaces. We further calculated the adsorption energy of HCHO, CO_2, O_2, H_2O and CO over two representative supported Pt/SiO$_2$ surfaces containing one platinum cluster of 13 atoms, namely, PtSiO$_2$-3.3 and PtSiO$_2$-4.6, with a silanol density of 3.3 and 4.6 OH nm^{-2}, respectively, at different adsorption sites: the top of the Pt$_{13}$ cluster and the interface between Pt$_{13}$ cluster and SiO$_2$ with different orientations. Here the Pt$_{13}$ cluster (the icosahedral cluster with 13 atoms) was chosen as a model to reflect the metal-support interactions due to its dynamic stability on silica surface and its size sufficiency to represent larger Pt NPs [43]. These new models have

been developed according to the methodology used in our previous works [44]. Computed adsorption energies in all cases are gathered in Table S3. These results show that the considered molecules are strongly adsorbed to the supported Pt$_{13}$ surfaces compared to the pure ones. On PtSiO$_2$-3.3 surface, O_2 prefers to interact via a dissociative mode with ΔE of − 490 kJ·mol^{-1}, where each oxygen atom interact with Pt$_{13}$ cluster surface via two Pt-O bonds, as illustrated in Fig. 7. HCHO is also dissociated under the effect of the surface but the adsorption in the molecule mode at the oxygen atom is more stable (−256 versus −270 kJ·mol^{-1}). CO tends to interact with Pt$_{13}$ cluster at the carbon atom while H_2O at the oxygen atom with ΔE of − 359 and − 317 kJ·mol^{-1}, respectively. CO_2 favours to interact with Pt$_{13}$ cluster at
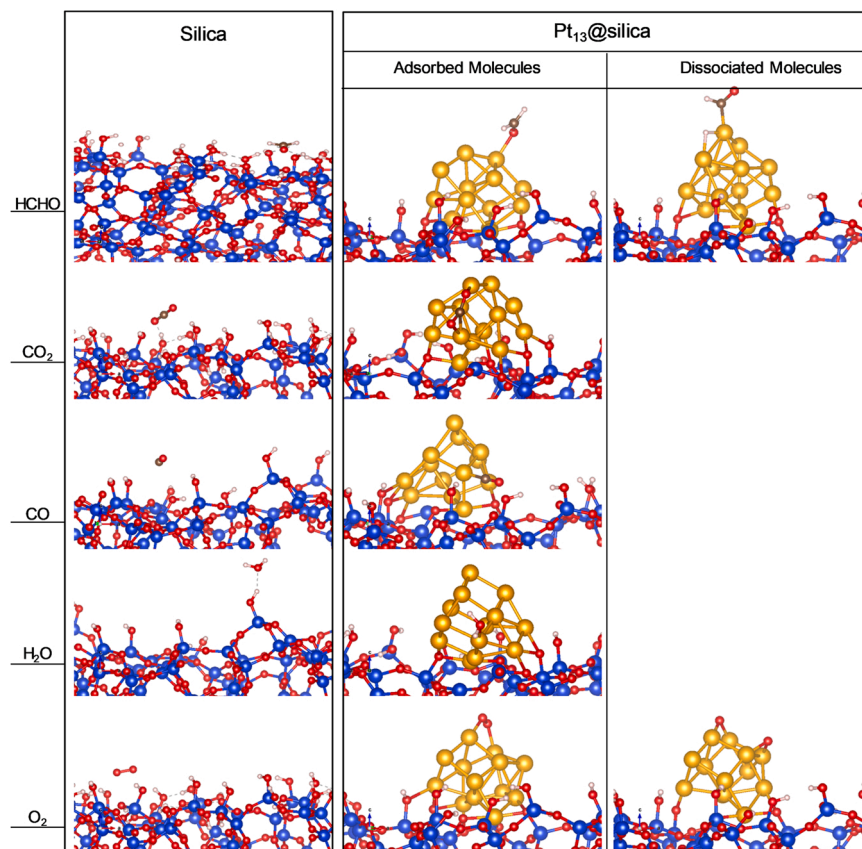
Fig. 7. The most favourable interaction modes of the considered molecules on pure silica and Pt$_{13}$ @SiO$_2$ surfaces.

both carbon and oxygen atoms with ΔE of -145 kJ·mol^{-1}. On PtSiO$_2$-4.6 surface, O$_2$, HCHO, CO, H$_2$O and CO$_2$ are apt to interact in the same adsorption geometry with PtSiO$_2$-3.3 but with much lower adsorption energy: -330, -200, -277, -93, and -59 kJ·mol^{-1}, respectively. The most favourable interaction modes of the considered molecules on PtSiO$_2$-4.6 and SiO$_2$-4.6 surfaces are summarized in Fig. 6b.

It is necessary to clarify that in the calculations here only surface silanol groups were considered for simplifying the study. However, in SiO$_2$-x and PtSiO$_2$-x (x = 2.3, 3.1), there also exist surface O-Si(CH$_3$)$_3$ groups that may play a role in affecting the adsorption behaviors of the gas molecules on catalyst surface during HCHO oxidation: (i) surface O-Si(CH$_3$)$_3$ groups could result in a steric hindrance due to their large group size, which could adversely affect the adsorption accessibility of HCHO and thus HCHO oxidation reactivity; (ii) surface O-Si(CH$_3$)$_3$ groups are repulsive to H$_2$O molecules due to their hydrophobicity, which could repress the adsorption of H$_2$O molecules on the active site surfaces. Based on the DFT calculations as revealed above, the O-Si(CH$_3$)$_3$-rich surface would have a similar influence to the silanol-poor surface: an increased difficulty for HCHO and H$_2$O adsorptive reactions. Thus though it is difficult to distinguish the contribution percentage of each one to the final results since O-Si(CH$_3$)$_3$ and silanols coexist, it is necessary to remind that the influence of surface silanol groups on gas molecules adsorption behaviours may also include in the contributions from the surface O-Si(CH$_3$)$_3$ groups. However, considering that surface silanols, instead of O-Si(CH$_3$)$_3$, may interact with and consume partial surface energy of Pt NPs [45], which could also affect the catalyst surface environment, the role of surface silanol is prior to O-Si(CH$_3$)$_3$.

3.5. Discussion

The catalytic performance of Pt/SiO$_2$ for HCHO oxidation depends on the dispersion of Pt NPs – high dispersion generally leads to high reactivity [16], the valent state of Pt species - high metallic Pt content benefits HCHO oxidation [15], and at last but not the least, the catalyst surface environment and notably the silanol density.

DFT calculations have indicated that contrary to the gas adsorption on the pure silica surfaces, the richest silanol Pt/SiO$_2$ surfaces significantly exhibit the lowest adsorption energies for all studied gas molecules and thus a weaker interaction with these molecules. The decreased adsorption strength with increased silanol density on Pt/SiO$_2$ could be reasonably assigned to the interaction of Pt NPs with the surface silanols of SiO$_2$ which consumed partial surface energy of Pt NPs. According to the Sabatier principle [46], neither the strongest nor the weakest, but the more moderate interaction strengths of reactants and intermediates benefits the high catalytic reactivity. Thus, the weakened adsorption strength of the mentioned gaseous molecules on silanol-rich Pt/SiO$_2$ surface may serve as an advantage to facilitate HCHO oxidation, and thus may be one of the reasons why in the dry air environment PtSiO$_2$-4.5 exhibited higher reactivity than PtSiO$_2$-3.1 and PtSiO$_2$-2.3.

Moreover, for PtSiO$_2$-3.3, only the inhibitory effect of CO$_2$ is negligible while CO, H$_2$O and O$_2$ act as the major inhibitors. Especially, the competitive adsorption of H$_2$O would decrease the active Pt surface and thus adversely affect HCHO oxidation. Interestingly, when the silanol density was raised to 4.6 OH nm^{-2}, though the adsorptive interaction of CO and O$_2$ with the Pt/SiO$_2$ surface still surpass that of HCHO, H$_2$O showing remarkably reduced adsorption energy ($\Delta E = -93$ kJ·mol^{-1}), tends to withdraw from the competitive adsorption on the active surface, which implies the lessening of the repressive effect of H$_2$O in OH-rich Pt@SiO$_2$ surface environment·H$_2$O as the product of HCHO oxidation would exist on the catalyst surface no matter in dry or wet air environment, thus the different adsorption behaviours of H$_2$O on OH-lacking and OH-rich Pt/SiO$_2$ surfaces would serve as another reason why PtSiO$_2$-2.3 and PtSiO$_2$-3.1 are less active than PtSiO$_2$-4.5.
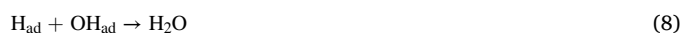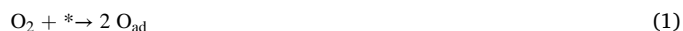
In addition, as aforementioned, the hydrophobicity of O-Si(CH$_3$)$_3$ groups may suppress H$_2$O molecules to adsorb on active sites and inhibit their activation into active OH species. This may serve as additional reasons why the silanol-poor (O-Si(CH$_3$)$_3$ - rich) Pt/SiO$_2$ samples exhibited less HCHO oxidation activity.

Providing insight into the reaction mechanism for HCHO oxidation, additional effects of the surface silanol environment on the catalytic reactivity could be revealed. The in situ DRIFTS spectra or time-dependent infrared spectra studies have frequently observed the methylenedioxy (DOM), formate species and CO as the main intermediates during HCHO oxidation over Pt supported catalysts on a variety of supports (i.e., SiO$_2$, TiO$_2$, MnO$_2$, AlOOH, Al$_2$O$_3$) [10,11,16,20,47]. Based on these well-established observations along with our DFT computing results and the experimental phenomenon, we can reasonably conclude the reaction pathways for HCHO oxidation over Pt/SiO$_2$ with various surface environments and humid conditions.

On Pt/SiO$_2$, Pt NPs are supposed to act as the only active sites. As revealed by DFT calculations, under dry air environment, the interaction strength of the gaseous molecules is in the following order: O$_2$ (dissociative adsorption) > CO (intermediate) > HCHO (molecule adsorption) > CO$_2$. O$_2$ molecules firstly adsorb on Pt surface and are activated into the dissociated O species (O$_{ad}$). O$_{ad}$ attacks the chemisorbed HCHO molecules and form DOM (H$_2$COO) [48]. This step is both thermodynamically and kinetically favourable due to the relatively low energy barrier and high energy release [49]. DOM then decomposes into formate (HCOO) and active hydrogen species (H$_{ad}$) [50]. H$_{ad}$ can migrate to a nearby O$_{ad}$ to form active hydroxyls (OH$_{ad}$). Besides, H$_2$O, either produced by HCHO or caught from the wet air, may also be activated by O$_{ad}$ to form OH$_{ad}$ [10]. Formate as an important intermediate would go through either a direct decomposition to form CO$_{ad}$, which then react with O$_{ad}$ to form CO$_2$, and OH$_{ad}$ which react with H$_{ad}$ to form H$_2$O; or formate can experience a more efficient reaction with OH$_{ad}$ or O$_{ad}$ to form CO$_2$ and H$_2$O directly [9–11,17,20,22,47,49].

These processes are summarized by Eqs. (1) to (9):

$$O_2 + * \rightarrow 2\,O_{ad} \tag{1}$$

$$HCHO_{ad} + O_{ad} \rightarrow H_2COO_{ad} \tag{2}$$

$$H_2COO_{ad} \rightarrow HCOO_{ad} + H_{ad} \tag{3}$$

$$HCOO_{ad} \rightarrow CO_{ad} + OH_{ad} \tag{4}$$

$$O_{ad} + H_2O \rightarrow OH_{ad} \tag{5}$$

$$HCOO_{ad} + OH_{ad} \rightarrow CO_2 + H_2O \tag{6}$$

$$H_{ad} + O_{ad} \rightarrow OH_{ad} \tag{7}$$

$$H_{ad} + OH_{ad} \rightarrow H_2O \tag{8}$$

$$CO_{ad} + O_{ad} \rightarrow CO_2 \tag{9}$$

* : adsorption sites; O$_{ad}$: adsorbed oxygen species; OH$_{ad}$: adsorbed hydroxyls; HCHO$_{ad}$: adsorbed HCHO; H$_2$COO$_{ad}$: adsorbed methylenediooxy species; HCOO$_{ad}$: adsorbed formate species; H$_{ad}$: adsorbed hydrogen species; CO$_{ad}$: adsorbed CO.

Clearly, H$_2$O plays an important role in HCHO oxidation. On one hand, its inhibitory effect on formaldehyde adsorption would have a negative effect on formaldehyde oxidation. On the other hand, it could act as source of active hydroxyl species which promote HCHO oxidation. As summarized in Scheme 1, in dry air environment and on silanol-rich surface, due to the relatively weak adsorption of H$_2$O on Pt/SiO$_2$ surface, the balance is tilted to the promotiing effect, which contributes to the high PtSiO$_2$-4.5 activity. In contrast, for silanol-lacking Pt/SiO$_2$ the adverse effect dominates, which results in their lower activity. In wet conditions, the role of H$_2$O becomes more significant. In this case, its promoting effect on HCHO oxidation would dominate whatever the silanol density since numerous active hydroxyl species derived from air H$_2$O decomposition are formed through Eq. (5). Moreover, the stronger
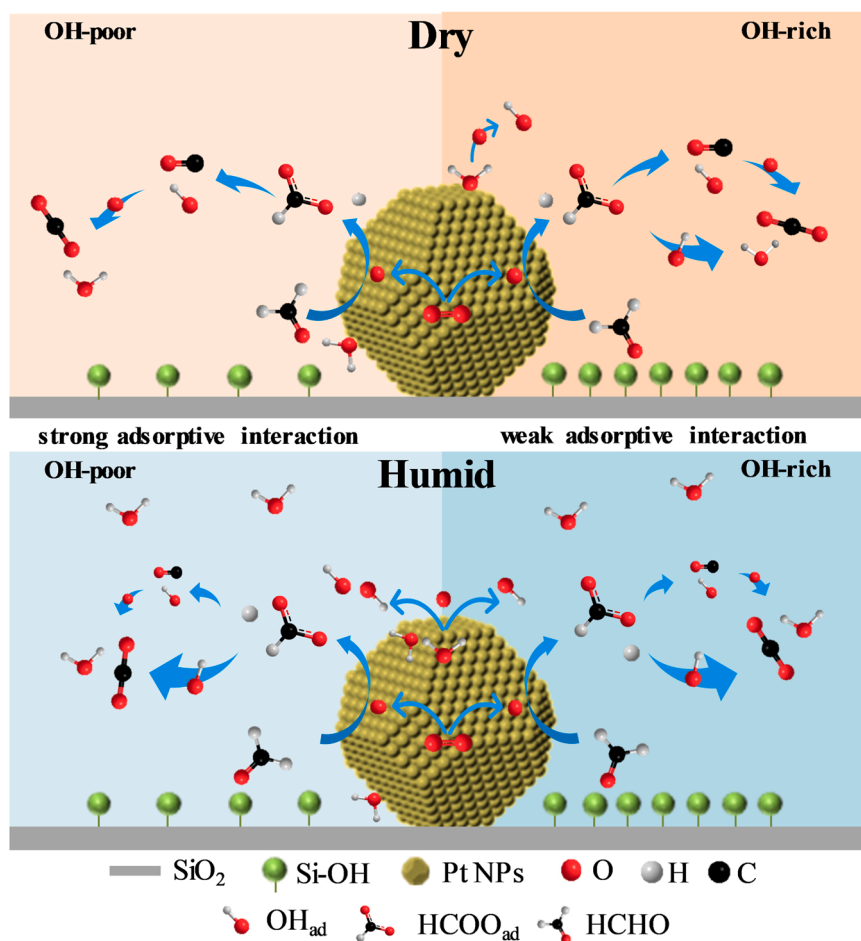
Scheme 1. HCHO oxidative decomposition mechanism for Pt/SiO$_2$ with different surface environment and humidity conditions. OH$_{ad}$: adsorbed hydroxyls; HCOO$_{ad}$: adsorbed formate species.

interaction of H$_2$O with silanol-lacking Pt/SiO$_2$ surface could drive more H$_2$O to be activated (into OH$_{ad}$). This could explain why the catalytic performance of all the Pt/SiO$_2$ samples was improved once increasing the air humidity and why the catalytic performance of the lowest silanol density Pt/SiO$_2$ sample increased more significantly. In addition, under humid conditions though the promotive effects of H$_2$O on HCHO oxidation dominate, H$_2$O's competitive adsorption against HCHO still remains, and its adverse effects would be higher at high humidity, considering the relatively weak H$_2$O activation capacity of PtSiO$_2$-4.5 [51,52]. This may explain the decrease in HCHO conversion with PtSiO$_2$-4.5 when the humidity was increased from 25% to 50% and 75%.

4. Conclusion

The present work investigated the catalytic performance of Pt/SiO$_2$ with tailored surface silanol densities in HCHO oxidation. Reactivity measurements show that the PtSiO$_2$-4.5 catalyst is highly efficient and stable in HCHO oxidation at room temperature (25 °C). Such good performance is attributed to the silanol-rich surface environment. Though it does not directly participate into the oxidation process of HCHO, the silanol groups play crucial roles in the interaction modes of molecules involved in the reaction. Special importance is given to water adsorption behaviours on different catalyst surface environments. The silanol-rich Pt/SiO$_2$ surface (e.g., 4.5 OH nm^{-2}) could reduce the interaction strength of water molecules (-93 kJ·mol^{-1} of ΔE (4.6 OH nm^{-2}) versus -317 kJ·mol^{-1} (ΔE (3.3 OH nm^{-2})) and thus their competitive adsorption with HCHO, benefiting HCHO decomposition. In humid environment, a suitable silanol density could properly increase

water interaction with catalyst surface, facilitate the water molecule activation and promote the catalytic performance in HCHO oxidation. The present work has not only shown for the first time in a straightforward way the effect of silanol density on the catalytic performance of Pt/SiO$_2$ in HCHO oxidation, but also has provided a new point of view to understand the critical role of surface hydroxyls in HCHO oxidation, and thus has shed light in the rational design of effective and low-cost catalysts for indoor formaldehyde removal.

CRediT authorship contribution statement

Shuo Chen: Investigation, Data curation, Formal analysis, Writing – original draft. **Saber Gueddida**: Investigation, Data curation, Formal analysis. **Michael Badawi**: Supervision, Validation, Writing – review & editing. **Sébastien Lebègue**: Validation, Writing – review & editing. **Jean-Marc Giraudon**: Visualization, Writing – review & editing. **Jérémy Dhainaut**: Visualization, Writing – review & editing. **Sébastien Royer**: Conceptualization, Supervision, Validation, Writing – review & editing. **Jean-Francois Lamonier**: Conceptualization, Supervision, Validation, Writing – review & editing, Funding acquisition, Project administration.

Declaration of Competing Interest

The authors declare that they have no known competing financial interests or personal relationships that could have appeared to influence the work reported in this paper.

Data Availability

Data will be made available on request.

Appendix A. Supporting information

Supplementary data associated with this article can be found in the online version at doi:10.1016/j.apcatb.2023.122672.

References

[1] C. Wang, Y. Li, C. Zhang, X. Chen, C. Liu, W. Weng, W. Shan, H. He, A simple strategy to improve Pd dispersion and enhance Pd/TiO$_2$ catalytic activity for formaldehyde oxidation: The roles of surface defects, Appl. Catal. B: Environ. 282 (2021) 119540, https://doi.org/10.1016/j.apcatb.2020.119540.

[2] C. He, J. Cheng, X. Zhang, M. Douthwaite, S. Pattisson, Z. Hao, Recent advances in the catalytic oxidation of volatile organic compounds: a review based on pollutant sorts and sources, Chem. Rev. 119 (2019) 4471–4568, https://doi.org/10.1021/acs.chemrev.8b00408.

[3] F. Liu, S. Rong, P. Zhang, L. Gao, One-step synthesis of nanocarbon-decorated MnO$_2$ with superior activity for indoor formaldehyde removal at room temperature, Appl. Catal. B: Environ. 235 (2018) 158–167, https://doi.org/10.1016/j.apcatb.2018.04.078.

[4] Z. Fan, J. Shi, Z. Zhang, M. Chen, W. Shangguan, Promotion effect of potassium carbonate on catalytic activity of Co3O4 for formaldehyde removal, J. Chem. Technol. Biotechnol. 93 (2018) 3562–3568, https://doi.org/10.1002/jctb.5733.

[5] H. Wang, W. Guo, Z. Jiang, R. Yang, Z. Jiang, Y. Pan, W. Shangguan, New insight into the enhanced activity of ordered mesoporous nickel oxide in formaldehyde catalytic oxidation reactions, J. Catal. 361 (2018) 370–383, https://doi.org/10.1016/j.jcat.2018.02.023.

[6] C. Ma, D. Wang, W. Xue, B. Dou, H. Wang, Z. Hao, Investigation of formaldehyde oxidation over Co$_3$O$_4$−CeO$_2$ and Au/Co$_3$O$_4$−CeO$_2$ catalysts at room temperature: effective removal and determination of reaction mechanism, Environ. Sci. Technol. 45 (2011) 3628–3634, https://doi.org/10.1021/es104146v.

[7] Y. Li, X. Chen, C. Wang, C. Zhang, H. He, Sodium enhances Ir/TiO$_2$ activity for catalytic oxidation of formaldehyde at ambient temperature, ACS Catal. 8 (2018) 11377–11385, https://doi.org/10.1021/acscatal.8b03026.

[8] Y. Li, C. Zhang, H. He, J. Zhang, M. Chen, Influence of alkali metals on Pd/TiO$_2$ catalysts for catalytic oxidation of formaldehyde at room temperature, Catal. Sci. Technol. 6 (2016) 2289–2295, https://doi.org/10.1039/C5CY01521A.

[9] M. Chen, W. Wang, Y. Qiu, H. Wen, G. Li, Z. Yang, P. Wang, Identification of active sites in HCHO oxidation over TiO$_2$-supported Pt catalysts, ACS Catal. 12 (2022) 5565–5573, https://doi.org/10.1021/acscatal.2c01150.

[10] Z. Liu, J. Niu, W. Long, B. Cui, K. Song, F. Dong, D. Xu, Highly efficient MnO$_2$/AlOOH composite catalyst for indoor low-concentration formaldehyde removal at room temperature, Inorg. Chem. 59 (2020) 7335–7343, https://doi.org/10.1021/acs.inorgchem.0c00852.

[11] Z. Yan, Z. Xu, J. Yu, M. Jaroniec, Enhanced formaldehyde oxidation on CeO$_2$/AlOOH-supported Pt catalyst at room temperature, Appl. Catal. B: Environ. 199 (2016) 458–465, https://doi.org/10.1016/j.apcatb.2016.06.052.

[12] T. Yang, Y. Huo, Y. Liu, Z. Rui, H. Ji, Efficient formaldehyde oxidation over nickel hydroxide promoted Pt/γ-Al$_2$O$_3$ with a low Pt content, Appl. Catal. B: Environ. 200 (2017) 543–551, https://doi.org/10.1016/j.apcatb.2016.07.041.

[13] Z. Yan, Z. Xu, B. Cheng, C. Jiang, Co$_3$O$_4$ nanorod-supported Pt with enhanced performance for catalytic HCHO oxidation at room temperature, Appl. Surf. Sci. 404 (2017) 426–434, https://doi.org/10.1016/j.apsusc.2017.02.010.

[14] S. Chen, C. Ciotonea, A. Ungureanu, E. Dumitriu, C. Catrinescu, R. Wojcieszak, F. Dumeignil, S. Royer, Preparation of nickel (oxide) nanoparticles confined in the secondary pore network of mesoporous scaffolds using melt infiltration, Catal. Today (2019), https://doi.org/10.1016/j.cattod.2019.01.064.

[15] N. An, W. Zhang, X. Yuan, B. Pan, G. Liu, M. Jia, W. Yan, W. Zhang, Catalytic oxidation of formaldehyde over different silica supported platinum catalysts, Chem. Eng. J. 215– 216 (2013) 1–6, https://doi.org/10.1016/j.cej.2012.10.096.

[16] H.C. Wu, T.C. Chen, Y.C. Chen, J.F. Lee, C.S. Chen, Formaldehyde oxidation on silica-supported Pt catalysts: The influence of thermal pretreatments on particle

[17] formation and on oxidation mechanism, J. Catal. 355 (2017) 87–100, https://doi.org/10.1016/j.jcat.2017.08.029.

[17] C. Zhang, F. Liu, Y. Zhai, H. Ariga, N. Yi, Y. Liu, K. Asakura, M. Flytzani-Stephanopoulos, H. He, Alkali-Metal-Promoted Pt/TiO$_2$ Opens a More Efficient Pathway to Formaldehyde Oxidation at Ambient Temperatures, Angew. Chem. Int. Ed. 51 (2012) 9628–9632, https://doi.org/10.1002/anie.201202034.

[18] L. Li, L. Li, L. Wang, X. Zhao, Z. Hua, Y. Chen, X. Li, X. Gu, Enhanced catalytic decomposition of formaldehyde in low temperature and dry environment over silicate-decorated titania supported sodium-stabilized platinum catalyst, Appl. Catal. B: Environ. 277 (2020), 119216, https://doi.org/10.1016/j.apcatb.2020.119216.

[19] Z. Yan, Z. Yang, J. Ouyang, A. Tang, In situ loading of highly-dispersed CuO nanoparticles on hydroxyl-group-rich SiO$_2$-AlOOH composite nanosheets for CO catalytic oxidation, Chem. Eng. J. 316 (2017) 1035–1046, https://doi.org/10.1016/j.cej.2017.02.043.

[20] S. Huang, B. Cheng, J. Yu, C. Jiang, Hierarchical Pt/MnO$_2$–Ni(OH)$_2$ hybrid nanoflakes with enhanced room-temperature formaldehyde oxidation activity, ACS Sustain. Chem. Eng. 6 (2018) 12481–12488, https://doi.org/10.1021/acssuschemeng.8b03139.

[21] L. Wang, H. Yue, Z. Hua, H. Wang, X. Li, L. Li, Highly active Pt/Na$_x$TiO$_2$ catalyst for low temperature formaldehyde decomposition, Appl. Catal. B: Environ. 219 (2017) 301–313, https://doi.org/10.1016/j.apcatb.2017.07.073.

[22] D.W. Kwon, P.W. Seo, G.J. Kim, S.C. Hong, Characteristics of the HCHO oxidation reaction over Pt/TiO2 catalysts at room temperature: the effect of relative humidity on catalytic activity, Appl. Catal. B: Environ. 163 (2015) 436–443, https://doi.org/10.1016/j.apcatb.2014.08.024.

[23] C.G. Okoye-Chine, C.O.L. Mbuya, T.S. Ntelane, M. Moyo, D. Hildebrandt, The effect of silanol groups on the metal-support interactions in silica-supported cobalt Fischer-Tropsch catalysts. A temperature programmed surface reaction, J. Catal. 381 (2020) 121–129, https://doi.org/10.1016/j.jcat.2019.10.036.

[24] J. Handzlik, K. Kurleto, M. Gierada, Computational insights into active site formation during alkene metathesis over a MoOx/SiO2 catalyst: the role of surface silanols, ACS Catal. 11 (2021) 13575–13590, https://doi.org/10.1021/acscatal.1c03912.

[25] H. Song, R.M. Rioux, J.D. Hoefelmeyer, R. Komor, K. Niesz, M. Grass, P. Yang, G.A. Somorjai, Hydrothermal growth of mesoporous SBA-15 silica in the presence of PVP-stabilized pt nanoparticles: synthesis, characterization, and catalytic properties, J. Am. Chem. Soc. 128 (2006) 3027–3037, https://doi.org/10.1021/ja057383r.

[26] P. Rupper, M. Amberg, D. Hegemann, M. Heuberger, Optimization of mica surface hydroxylation in water vapor plasma monitored by optical emission spectroscopy, Appl. Surf. Sci. 509 (2020), 145362, https://doi.org/10.1016/j.apsusc.2020.145362.

[27] J. Xu, S. Li, W. Zhang, S. Yan, C. Liu, X. Yuan, X. Ye, H. Li, The impact of deposition and annealing temperature on the growth properties and surface passivation of silicon dioxide films obtained by atomic layer deposition, Appl. Surf. Sci. 544 (2021), 148889, https://doi.org/10.1016/j.apsusc.2020.148889.

[28] X. Yu, J. Zhang, X. Wang, Q. Ma, X. Gao, H. Xia, X. Lai, S. Fan, T.S. Zhao, Fischer-Tropsch synthesis over methyl modified Fe$_2$O$_3$@SiO$_2$ catalysts with low CO$_2$ selectivity, Appl. Catal. B: Environ. 232 (2018) 420–428, https://doi.org/10.1016/j.apcatb.2018.03.048.

[29] G. Li, Y.C. He, P.L. Zhu, T. Zhao, R. Sun, D. Lu, C.P. Wong, Tailored surface chemistry of SiO$_2$ particles with improved rheological, thermal-mechanical and adhesive properties of epoxy based composites for underfill applications, Polymer 156 (2018) 111–120, https://doi.org/10.1016/j.polymer.2018.09.063.

[30] R. Mueller, H.K. Kammler, K. Wegner, S.E. Pratsinis, OH surface density of SiO$_2$ and TiO$_2$ by thermogravimetric analysis, Langmuir 19 (2003) 160–165, https://doi.org/10.1021/la025785w.

[31] D.W. Sindorf, G.E. Maciel, Cross-polarization magic-angle-spinning silicon-29 nuclear magnetic resonance study of silica gel using trimethylsilane bonding as a probe of surface geometry and reactivity, J. Phys. Chem. 86 (1982) 5208–5219, https://doi.org/10.1021/j100223a029.

[32] M. Thommes, K. Kaneko, A.V. Neimark, J.P. Olivier, F. Rodriguez-Reinoso, J. Rouquerol, K.S.W. Sing, Physisorption of gases, with special reference to the evaluation of surface area and pore size distribution (IUPAC technical report), Pure Appl. Chem. 87 (2015) 1051–1069, https://doi.org/10.1515/pac-2014-1117.

[33] J. Zhang, R.K. Gupta, C.A. Wilkie, Controlled silylation of montmorillonite and its polyethylene nanocomposites, Polymer 47 (2006) 4537–4543, https://doi.org/10.1016/j.polymer.2006.04.057.

[34] G. Chen, Y. Zhao, G. Fu, P.N. Duchesne, L. Gu, Y. Zheng, X. Weng, M. Chen, P. Zhang, C.-W. Pao, J.-F. Lee, N. Zheng, Interfacial effects in iron-nickel hydroxide–platinum nanoparticles enhance catalytic oxidation, Science 344 (2014) 495–499, https://doi.org/10.1126/science.1252553.

[35] C. Chen, F. Chen, L. Zhang, S. Pan, C. Bian, X. Zheng, X. Meng, F.S. Xiao, Importance of platinum particle size for complete oxidation of toluene over Pt/ZSM-5 catalysts, Chem. Commun. 51 (2015) 5936–5938, https://doi.org/10.1039/C4CC09383F.

[36] X. Chen, X.B. Wang, S. Han, D. Wang, C. Li, W. Guan, W.-Y. Li, C. Liang, Overcoming limitations in the strong interaction between Pt and irreducible SiO2 enables efficient and selective hydrogenation of anthracene, ACS Appl. Mater. Interfaces 14 (2022) 590–602, https://doi.org/10.1021/acsami.1c16965.

[37] A. Poursaeidesfahani, E. Andres-Garcia, M. de Lange, A. Torres-Knoop, M. Rigutto, N. Nair, F. Kapteijn, J. Gascon, D. Dubbeldam, T.J.H. Vlugt, Prediction of adsorption isotherms from breakthrough curves, Microporous Mesoporous Mater. 277 (2019) 237–244, https://doi.org/10.1016/j.micromeso.2018.10.037.

[38] C. Iuga, A. Vivier-Bunge, A. Hernández-Laguna, C.I. Sainz-Díaz, Quantum chemistry and computational kinetics of the reaction between OH radicals and formaldehyde adsorbed on small silica aerosol models, J. Phys. Chem. C. 112 (2008) 4590–4600, https://doi.org/10.1021/jp077557m.

[39] J.-P. Bellat, G. Weber, I. Bezverkhyy, J.-F. Lamonier, Selective adsorption of formaldehyde and water vapors in NaY and NaX zeolites, Microporous Mesoporous Mater. 288 (2019), 109563, https://doi.org/10.1016/j.micromeso.2019.109563.

[40] S. Gueddida, M. Badawi, H.E. Reynel-Ávila, A. Bonilla-Petriciolet, S. Lebègue, Selective adsorption of glucose towards itaconic acid on amorphous silica surfaces: Insights from density functional theory calculations, J. Mol. Liq. 343 (2021), 117586, https://doi.org/10.1016/j.molliq.2021.117586.

[41] S. Gueddida, S. Lebègue, M. Badawi, Assessing the potential of amorphous silica surfaces for the removal of phenol from biofuel: a density functional theory investigation, J. Phys. Chem. C. 124 (2020) 20262–20269, https://doi.org/10.1021/acs.jpcc.0c06581.

[42] A. Comas-Vives, Amorphous SiO_2 surface models: energetics of the dehydroxylation process, strain, ab initio atomistic thermodynamics and IR spectroscopic signatures, Phys. Chem. Chem. Phys. 18 (2016) 7475–7482, https://doi.org/10.1039/C6CP00602G.

[43] C.S. Ewing, M.J. Hartmann, K.R. Martin, A.M. Musto, S.J. Padinjarekutt, E. M. Weiss, G. Veser, J.J. McCarthy, J.K. Johnson, D.S. Lambrecht, Structural and electronic properties of Pt13 nanoclusters on amorphous silica supports, J. Phys. Chem. C. 119 (2015) 2503–2512, https://doi.org/10.1021/jp5105104.

[44] S. Gueddida, M. Badawi, T. Aminabhavi, S. Lebègue, Competitive adsorption of phenol and toluene onto silica-supported transition metal clusters for biofuel purification, Mol. Syst. Des. Eng. 6 (2021) 817–824, https://doi.org/10.1039/D1ME00046B.

[45] N. Debons, D. Dems, T. Coradin, C. Aimé, Mapping organic functional groups at nanosurfaces using colloidal gold conjugation, Nanoscience (2021), https://doi.org/10.26434/chemrxiv.13712311.v1.

[46] S. Hu, W.-X. Li, Sabatier principle of metal-support interaction for design of ultrastable metal nanocatalysts, Science 374 (2021) 1360–1365, https://doi.org/10.1126/science.abi9828.

[47] Z. Xu, J. Yu, M. Jaroniec, Efficient catalytic removal of formaldehyde at room temperature using AlOOH nanoflakes with deposited Pt, Appl. Catal. B: Environ. 163 (2015) 306–312, https://doi.org/10.1016/j.apcatb.2014.08.017.

[48] H. Huang, X. Ye, H. Huang, L. Zhang, D.Y.C. Leung, Mechanistic study on formaldehyde removal over Pd/TiO_2 catalysts: oxygen transfer and role of water vapor, Chem. Eng. J. 230 (2013) 73–79, https://doi.org/10.1016/j.cej.2013.06.035.

[49] S. Li, X. Lu, W. Guo, H. Zhu, M. Li, L. Zhao, Y. Li, H. Shan, Formaldehyde oxidation on the $Pt/TiO_2(101)$ surface: a DFT investigation, J. Organomet. Chem. 704 (2012) 38–48, https://doi.org/10.1016/j.jorganchem.2012.01.002.

[50] Y. Bu, Y. Chen, G. Jiang, X. Hou, S. Li, Z. Zhang, Understanding of $Au-CeO_2$ interface and its role in catalytic oxidation of formaldehyde, Appl. Catal. B: Environ. 260 (2020), 118138, https://doi.org/10.1016/j.apcatb.2019.118138.

[51] Y. Ishikawa, M.-S. Liao, C.R. Cabrera, Energetics of H2O dissociation and COads+ OHads reaction on a series of Pt–M mixed metal clusters: a relativistic density-functional study, Surf. Sci. 513 (2002) 98–110, https://doi.org/10.1016/S0039-6028(02)01697-7.

[52] S.-F. Peng, J.-J. Ho, The adsorption and dissociation of H2O on TiO2(110) and M/TiO2(110) (M = Pt, Au) surfaces–a computational investigation, Int. J. Hydrog. Energy 35 (2010) 1530–1536, https://doi.org/10.1016/j.ijhydene.2009.12.066.